Astronomy & Astrophysics manuscript no. articleRXJ
June 5, 2009

A joint spectro-imaging analysis of the *XMM-Newton* and HESS observations of the supernova remnant RX J1713.7-3946

F. Acero[1], J. Ballet[1], A. Decourchelle[1], M. Lemoine-Goumard[2,3], M. Ortega[4], E. Giacani[4], G. Dubner[4], G. Cassam-Chenaï[5].

1: Laboratoire AIM, CEA/DSM-CNRS-Université Paris Diderot, IRFU/SAp, CEA-Saclay, 91191 Gif sur Yvette, France
e-mail: fabio.acero@cea.fr
2: CNRS/IN2P3, Centre d'Etudes nucléaires de Bordeaux Gradignan, UMR 5797, Gradignan 33175, France
3: Université Bordeaux I, Centre d'Etudes nucléaires de Bordeaux Gradignan, UMR 5797, Gradignan 33175, France
4: Instituto de Astronomía y Física del Espacio (IAFE), CC 67, Suc. 28, 1428 Buenos Aires, Argentina
5: INAF-Osservatorio Astrofisico di Arcetri, Largo E. Fermi, 5, 50125 Firenze, Italy

Received 19 december 2008 / Accepted 31 May 2009

ABSTRACT

Context. The supernova remnant (SNR) RX J1713.7-3946 (also known as G347.3-0.5) is part of the class of remnants dominated by synchrotron emission in X-rays. It is also one of the few shell-type SNRs observed at TeV energies allowing to investigate particle acceleration at SNRs shock.
Aims. Our goal is to compare spatial and spectral properties of the remnant in X- and γ-rays to understand the nature of the TeV emission. This requires to study the remnant at the same spatial scale at both energies. To complement the non-thermal spectrum of the remnant, we attempt to provide a reliable estimate for the radio flux density.
Methods. In radio, we revisited ATCA data and used HI and mid-infrared observations to disentangle the thermal from the non-thermal emission. In X-rays, we produced a new mosaic of the remnant and degraded the spatial resolution of the X-ray data to the resolution of the HESS instrument to perform spatially resolved spectroscopy at the same spatial scale in X- and γ-rays. Radial profiles were obtained to investigate the extension of the emission at both energies.
Results. We found that part of the radio emission within the SNR contours is thermal in nature. Taking this into account, we provide new lower and upper limits for the integrated synchrotron flux of the remnant at 1.4 GHz of 22 Jy and 26 Jy respectively. In X-rays, we obtained the first full coverage of RX J1713.7-3946 with *XMM-Newton*. The spatial variation of the photon index seen at small scale in X-rays is smeared out at HESS resolution. A non-linear correlation between the X- and γ-ray fluxes of the type $F_{\rm X} \propto F_{\gamma}^{2.41}$ is found. If the flux variation are mainly due to density variation around the remnant then a leptonic model can more easily reproduce the observed X/γ-ray correlation. In some angular sectors, radial profiles indicate that the bulk of the X-ray emission comes more from the inside of the remnant than in γ-rays.

Key words. ISM: supernova remnants – Supernovae : individuals : RX J1713.7-3946 – Acceleration of particles

1. Introduction

Supernova remnants (SNRs) have long been believed to be accelerators of cosmic rays at least up to the *knee* ($\sim 10^{15}$ eV). Evidence that electrons are indeed accelerated in SNRs is found both in radio and X-rays through synchrotron emission. The detection of TeV emission from a SNR is an evidence of proton acceleration if the γ-rays come from the interaction of accelerated protons with the ambient matter (hadronic model). However the γ-rays can also be produced via Inverse Compton scattering (IC) of accelerated TeV electrons off ambient photons (leptonic model) that could be either infrared surrounding emission or cosmic microwave background. The SNRs interacting with dense molecular clouds are good candidates to detect γ-ray emission from the hadronic mechanism as the high density of the cloud provides a large amount of targets for the accelerated protons. The SNR RX J1713.7-3946 (also known as G347.3-0.5) is one of those candidates as it is interacting with a dense molecular cloud in the northwest (NW) and in the southwest (SW) of the remnant (Fukui et al. 2003; Cassam-Chenaï et al. 2004; Moriguchi et al. 2005).

RX J1713.7-3946 was first discovered in X-rays with the ROSAT all-sky survey in 1996 (Pfeffermann & Aschenbach 1996). The remnant is close to the galactic plane and its distance is controversial. Using ASCA observations and the measurement of the column density toward the source, it was first proposed to be at a distance of 1 kpc (Koyama et al. 1997). Then Slane et al. (1999) derived a distance of 6 kpc based on a possible association of the remnant with molecular clouds and the HII region G347.611+0.204. The comparison of the X-ray and HI absorbing column densities (Cassam-Chenaï et al. 2004) as well as CO observations of a molecular cloud interacting with the remnant (Fukui et al. 2003) both suggest a closer distance of 1 kpc (value adopted in this paper). In this case, the remnant is about 20 pc in diameter (70 arcmin on the sky) and could be associated with the supernova that exploded in AD 393 in the tail of the constellation Scorpius (Wang et al. 1997). The remnant would then be about 1600 years old.
In the radio band Slane et al. (1999) showed for the first time an image of RX J1713.7-3946, based on MOST observations at 843 MHz. Later on, Ellison et al. (2001) and Lazendic et al. (2004) (with a recalibrated and improved image) reported ATCA radio observations of this SNR at 1.4 GHz (left-hand panel of

Fig. 5). The SNR appears as a faint nebula ($\sim 1^\circ$ in diameter) with many short, curved features, the brightest of which are the two bright arcs visible on the northwest corner. These arcs coincide with the edges of the brightest X-ray emission. Interestingly, those arcs are observed to be in the vicinity of the HII region G347.611+0.204 which is located at 6.6 kpc (Russeil 2003; Conti & Crowther 2004). An almost complete ring of weak emission, about 30 arcmin in size, can be also detected near the center of this extended SNR. An accurate estimate of the integrated radio flux density of RX J1713.7-3946 is a pending problem. This is due to the intrinsic faintness of this SNR, the possible mixing of the SNR synchrotron emission with the thermal emission of the nearby HII region as well as the limited quality of the available data.

In X-rays the emission is dominated by a non-thermal continuum and no emission lines have been observed so far (Koyama et al. 1997; Slane et al. 1999; Pannuti et al. 2003; Cassam-Chenaï et al. 2004). This non detection can set an upper limit to the ionization age. Assuming $t_{SNR} = 1600$ yrs an upper limit on the density of the ambient medium of 0.02 cm^{-3} is then derived (Cassam-Chenaï et al. 2004). The study of the remnant with *XMM-Newton* at small spatial scale carried out by Cassam-Chenaï et al. (2004) and Hiraga et al. (2005) clearly showed a spatial variation of the photon index. It varies from 1.9 to 2.6 with a mean statistical error of 4% (Cassam-Chenaï et al. 2004). A correlation between the X-ray flux and the photon index is also observed. Those results were obtained using an adaptive grid to have approximately the same number of counts in each pixel grid region where a spectrum is then extracted. On the bright regions (the north-west rim), the size of the grid pixel is typically 0.05°.

In γ-rays, RX J1713.7-3946 has been detected by the CANGAROO collaboration (Muraishi et al. 2000; Enomoto et al. 2002). It was then definitely established by the HESS telescopes which provided the first spatially resolved γ-ray image of the remnant (Aharonian et al. 2004). The overall morphology is very similar to that in X-rays (same western shell) and the brightest spots (located to the north-west) are coincident. As the remnant is extended and is the brightest shell-type SNR seen in γ-rays, its emission can be studied in detail. With the good spatial resolution of the HESS telescopes ($\sim 0.1^\circ$) it has been possible to carry out a spatially resolved spectral study at large scale (Aharonian et al. 2006, hereafter AH06). No evidence for spatial variations of the photon index from region to region (mean value of 2.09 and a standard deviation of 0.07) was found down to the precision of the measurements (mean 1σ statistical error of $\pm$ 0.08). Moreover there does not seem to be any correlation between the γ-ray flux and the photon index (Fig. 14 of AH06).

Those γ-ray results are very different from what has been found at small scale in X-rays. However it is important to note that the X- and γ-rays results were not obtained looking at the same spatial scale (the spectra were not extracted using the same size of extraction regions). Moreover the Point Spread Function of both instruments is very different. Those differences hamper a comparison of the results at both energies. The major issue here is whether the spectral parameters are really different in X- and γ-rays or if this difference is introduced by the fact that both studies are looking at different spatial scales.

To investigate this question we carried out a detailed comparison of the remnant in X- and γ-rays using the same extraction regions and taking into account the different spatial resolution of the two instruments. We compared both the spectral properties of the remnant and the morphology using radial profiles in X- and γ-rays.

Concerning the radio flux estimate, we investigated which part of the radio emission is synchrotron emission in origin (related to the remnant) or thermal emission (possibly related to the nearby HII region). We then calculated the integrated flux density re-analysing Lazendic et al. (2004)'s database.

In Sect. 2, we present the different sets of data used in this study including the new *XMM-Newton* observations that complete the mosaic of the remnant. Section 3 presents the methods used for the processing of the X-ray data. In Sect. 4, the estimate of the integrated radio flux of the remnant and the results of the X- and γ-ray spectral and morphological comparison are shown. In Sect. 5, we discuss this comparison in the framework of an hadronic and leptonic model. The implications of the new radio flux for the multi-wavelength emission models of the remnant are also discussed.

2. Data

2.1. Radio data

In this work we re-analyzed ATCA observations carried out at 1.4 GHz (Lazendic et al. 2004) following different paths to estimate the radio flux density of RX J1713.7-3946. The details to carry out an accurate calculation are discussed in Sect. 4.1.

2.2. Infrared data

Infrared observations in and around the remnant can help disentangling the thermal from the non thermal radio emission which is crucial to estimate the radio flux of the whole remnant. We used a method based on a color-color criteria proposed by Reach et al. (2006) using *Spitzer* data at 3.6, 4.5, 5.8, and 8 μm from the Galactic Legacy Infrared Mid-Plane Survey Extraordinaire (GLIMPSE, Benjamin et al. 2003). The spatial resolution of the survey is about 2 arcsec. More details can be found in Sect. 4.1.

2.3. XMM-Newton data

The first set of observations of the SNR RX J1713.7-3946 (presented in Cassam-Chenaï et al. 2004) covered almost the entire remnant. New observations of the south, east and west regions completed the mosaic of the remnant. With a total of 11 pointings (see Table 1) we can now provide the first full mapping of RX J1713.7-3946 with *XMM-Newton* (see Fig. 1).

To clean proton flare contamination in the event files, we built a histogram of counts/seconds in the 10-12 keV band for the MOS cameras (12-14 keV for PN). Then we fit a gaussian distribution upon the histogram and retain, in the observation, only the time intervals where the count rates are within a 3σ range (Pratt & Arnaud 2002). Table 1 provides the list of the remaining exposure times after flare screening. For the PN instrument only 6 pointings were used.

2.4. HESS data

In the HESS study (AH06) spectra were extracted from 14 square regions (0.26° length, see Fig. 2) covering the whole remnant. The data used for the spectral analysis have a cut on the minimum size of image of 80 photo-electrons resulting on a mean spatial resolution of 0.12° (68% containment radius). For the morphological analysis (radial profile) the cut used in HESS

data is at 200 photo-electrons resulting on a better spatial resolution of 0.08°. The detection efficiency varies over the 5° of the full field of view but it is almost constant at the scale of the remnant which is ∼ 1° wide (it varies by only 5% between the centre and the edge of the object). All the data used in our study are taken from AH06 and we did not reprocess any TeV data. For the comparison of the spectral properties we used the γ-ray results presented in Table 2 of AH06 and for the comparison of radial profile we used the data presented in Fig. 16.

3. X-ray processing

3.1. Mosaic construction

The mosaic is built in counts and an adaptive smoothing is applied such that the signal-to-noise ratio is at least 10. The instrumental background is derived from a compilation of blank sky observations (Carter & Read 2007), renormalized in the 10-12 keV energy band for the MOS cameras (12-14 keV for PN) and subtracted from each image. To have units in photons/cm^2/s/pixel instead of counts/s/pixel, the exposure map of each observation is multiplied by the average effective area in the energy band (assuming the same spectrum over the field of view). Then a mosaic of those exposure maps is built and smoothed in the same way. The final image is the division of the counts mosaic by the exposure map mosaic.
The resulting image which is the sum of the MOS and available PN data after flare screening is presented in Fig. 1. The morphology of RX J1713.7-3946 can be decomposed in two main kinds of structures : diffuse emission present over all the remnant and bright filaments particularly visible in the west and north of the remnant (see Fig. 1). Thanks to the high sensitivity of *XMM-Newton*, we can clearly see the faint emission in the recent observations of the regions south, east and north. In particular in the northern region of the remnant we distinctly see a straight edge that is not an artifact due to a CCD gap or any instrumental effect. Also it is not due to an X-ray absorption along the line of sight as this straight edge remains visible on the 4.5-7.5 keV image (in this energy band the absorption is weak). Simply the emission seems fainter there. Above that edge, we see a structure (in blue-green) that seems to be the continuity of the shock.

The estimate of the astrophysical background is not simple in RX J1713.7-3946 as it seems to vary around the remnant. However in order to have a rough approximation of the background level we extracted the flux outside a circle of 0.56° radius centered on the remnant (α_{J2000} =17h13m46s, δ_{J2000} = −39°44′56”). We then subtracted the mean value of this flux (4.5×10^{-6} photons/cm^2/s/arcmin^2) for the morphological study. The small structures of the SNR are not affected by this background subtraction.

3.2. Spectral extraction method

With its good spatial resolution, the *XMM-Newton* telescope can carry out spectral study at small scale whereas in γ-rays the spectral analysis is done at larger scale due to the comparatively lower spatial resolution of the HESS telescopes. To address this problem, we took into account the different Point Spread Functions and the variation of the detection efficiency across the field of view of the two instruments.

In the case of *XMM-Newton*, the detection efficiency of the MOS and PN cameras can drop 35% from the centre to the edge of our 0.26° extraction regions. For the HESS telescopes the detection efficiency is almost constant to this size (see Sect 2.4).

Table 1. *XMM-Newton* observations used in this paper. The total and good columns represent the exposure time before and after flare screening.

		Exposure (ks)		
		MOS		PN
ObsId	Observation Date	Total	Good	Good
0093670101 (NE)	2001 September 5	15.3	1.8	0
0093670201 (NW)	2001 September 5	15.3	6.7	0
0093670301 (SW)	2001 September 8	15.3	15.2	10.0
0093670401 (SE)	2002 March 14	14.1	11.6	5.1
0093670501 (CE)	2001 March 2	13.8	13.0	6.5
0207300201 (CE)	2004 February 22	31.5	12.4	0.
0203470401 (NE)	2004 March 25	17.0	16.1	6.7
0203470501 (NW)	2004 March 25	18.0	13.1	9.7
0502080101 (E)	2007 September 15	34.6	5.8	0
0502080301 (W)	2007 October 3	8.9	2.8	0
0551030101 (S)	2008 September 27	24.9	24.5	20.8

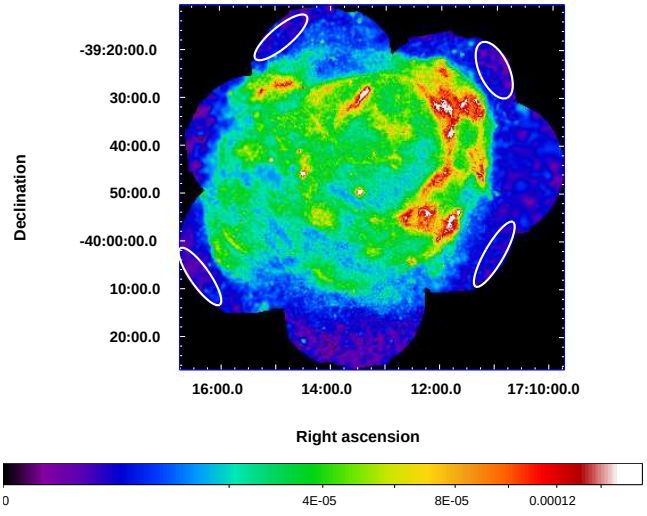

Fig. 1. EPIC MOS plus PN image in the 0.5-4.5 keV band. The units are ph/cm^2/s/arcmin^2 and the scale is square root. The image was adaptively smoothed to a signal-to-noise ratio of 10. The four ellipses show the regions used to estimate the local astrophysical background for the spectral analysis.

When extracting an X-ray spectrum in this large region we want all the events to contribute with the same weight to the spectrum. To address this problem, we used the weight method described in Arnaud et al. (2001) where each event is corrected for its efficiency loss as a function of its position on the camera and its energy.

We also have to take into account the different size of the Point Spread Function of both instruments. For the spectral study of this SNR, the mean spatial resolution of the HESS instrument is 0.12° (68% containment radius) which is comparable to the size of the extraction region (0.26°) whereas with the *XMM-Newton* observatory, the spatial resolution is about 7 arcsecs.

We assumed that the Point Spread Function of the HESS telescopes is a gaussian of σ = 0.0795° (corresponding to the HESS 68% containment radius of 0.12°) and that in comparison the Point Spread Function of *XMM-Newton* is negligible. To decrease the spatial resolution of the X-ray data, we redistributed

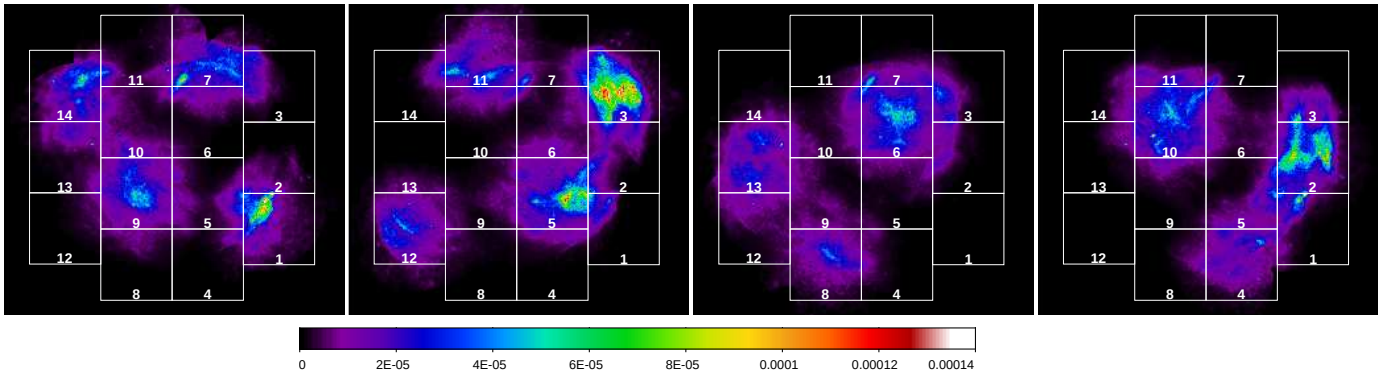

Fig. 2. Spatial X-ray contribution to each HESS region (as defined in Aharonian et al. (2006)). We see that due to the size of the PSF comparable with the size of the extraction regions, many events outside of the region contribute to the spectrum. To save space, each frame shows the contributions to three or four separate regions at once. The linear scale is in ph/cm^2/s/arcmin^2. The regions 1 to 14 defined here are used later for the spectral analysis in Table 2, Fig. 7, 8 and 9.

randomly the position of each X-ray event according to the gaussian probability density function.

For the purpose of spectral comparison with the γ-rays, we removed the two following very bright point-like sources in the X-ray data : 1WGA J1713.4-3949 which is argued to be the Central Compact Object of the SNR (Slane et al. 1999; Lazendic et al. 2003; Cassam-Chenaï et al. 2004) and 1WGA J1714.4-3945 which is associated with a star (Pfeffermann & Aschenbach 1996).

3.3. X-ray background spectra

The instrumental background spectrum is derived from blank sky observations (Carter & Read 2007) in the same detector area, renormalized in the 10-12 keV energy band for the MOS cameras (12-14 keV for PN) and processed with the same method as the observations (see Sect. 3.2).

The subtraction of the local astrophysical background, is not a simple problem in RX J1713.7-3946. On the one hand, as the remnant is $\sim 1^\circ$ in size and close to the galactic plane, the local astrophysical emission can vary around the remnant. On the other hand, there are only few pointings that allow us to estimate this background. We extracted background spectra outside of the SNR in 4 regions where the statistics was sufficient (see the 4 ellipses in Fig. 1). In this astrophysical background, no emission lines are seen but the statistics is low. For comparing the spectral properties of the background between the different regions, we modeled the spectra using a simple absorbed power law model. The parameters of this model are similar in the northern, north-western and south-western regions i.e. : $N_{\rm H} \simeq 0.4 \times 10^{22}$ cm^{-2}, index $\simeq 1.9$ and a normalization *norm* $\simeq 1.4 \times 10^{-3}$ keV^{-1}cm^{-2}s^{-1} at 1 keV (renormalized to the area of the large HESS extraction regions). Note that in the south-eastern region, the normalization parameter is 40 % smaller. As all the extracted background spectra have low statistics, we decided to use a power law model with the parameters listed above for the astrophysical background instead of a spectrum. We used the same $N_{\rm H}$, index and normalization parameters that of the northern, north-western and south-western regions for all the extraction regions. The impact of such a choice for the south-eastern region, where the normalization is smaller, is discussed later in Sect. 3.4.

3.4. Spectral modeling

The X-ray emission of the remnant is dominated by a non-thermal continuum and no emission lines have been detected so far (Koyama et al. 1997; Slane et al. 1999; Pannuti et al. 2003; Cassam-Chenaï et al. 2004). In our study, all spectra are well described by an absorbed power law model as is illustrated in Fig. 3. In some observations, the PN instrument exposure time was null after flare screening. To have an homogeneous coverage of the remnant we kept only the MOS data. Whenever it was possible we fitted independently, as a test, the spectrum extracted from the MOS1&2 and PN instruments and compared the resulting best-fit parameters. They agreed within the statistical errors bars.
All the data was fitted using unbinned spectra with the C-statistic implemented in Xspec (v12.3.1). Binning was used for graphical purposes only and fixed at 3σ for all spectra. We have fitted all the data from 0.8 keV to 10 keV. The best-fit parameters for the HESS regions are listed in Table 2. As discussed in Sect. 3.3, the local astrophysical background in the south-eastern region seems weaker than the average background used for all the regions. Therefore, we studied the impact of those different backgrounds for the faintest region (the most dependant to background subtraction) which is located in the SE : region 12. When using a value of the normalization parameter 40 % smaller for the background model, the new best-fit parameters do not vary much. While the hydrogen column and the index change within the errors bars, the integrated X-ray flux varies by less than 10%. As the variations are small and do not impact the results of our study, we kept the same astrophysical background for all the regions.

3.5. Radial profile method

As we now have a full coverage of the remnant, we can properly compare the radial profiles of the emission of the remnant in X- and γ-rays. To match the HESS spatial resolution we smoothed the X-ray image with a gaussian of σ=0.053° (corresponding to $r_{68\%}$=0.08°). We then extracted a flux per unit solid angle as function of the distance to the center on the smoothed X-ray images (1-2 keV and 2-4.5 keV band) in eight sectors as shown in Fig. 4. To compare the radial profiles at both wavelengths, the X-ray profiles were scaled by a unique normalisation factor calculated as the ratio of the total number of counts in γ-rays over the total flux in X-rays on the whole remnant. In the last two

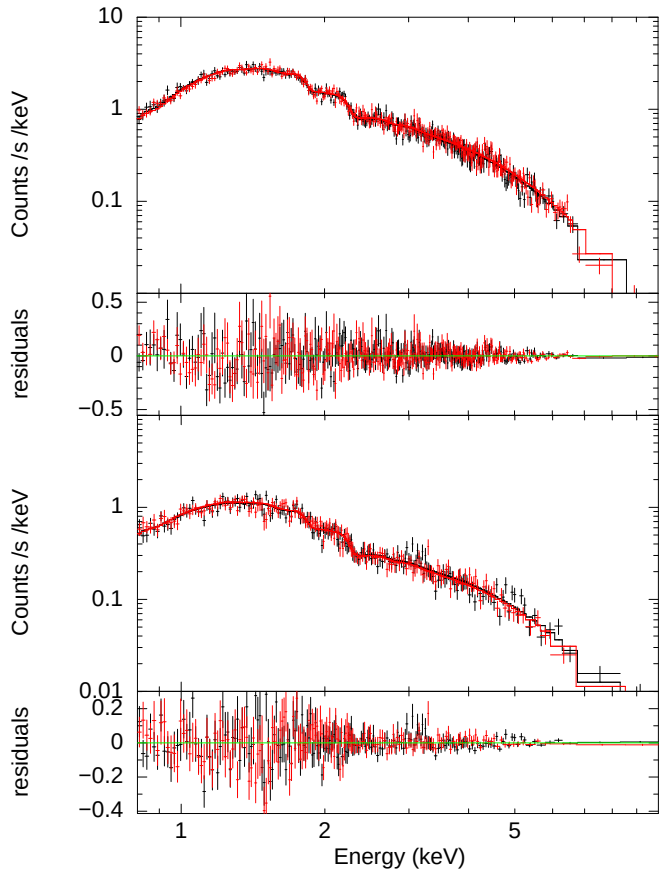

Fig. 3. Best-fit X-ray spectrum from region 3 (*Top* panel) and region 12 (*Bottom* panel) with an absorbed power law model (MOS1 spectrum is in black and MOS2 in red). The region 3, located on the north-west, is the brightest region of the remnant. It has a steep spectrum (2.35) and has a high absorption (0.72×10^{22}cm^{-2}). On the south-east of the remnant, region 12 is faint, has a weak absorption (0.50×10^{22}cm^{-2}) and has a harder spectrum (2.17).

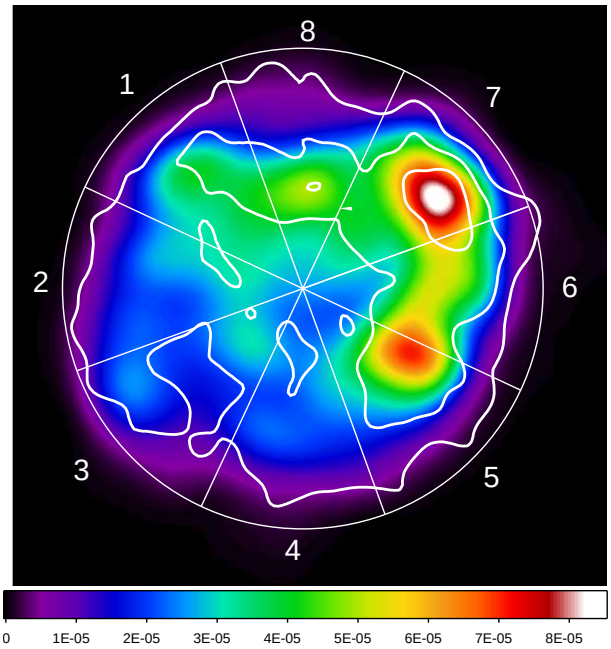

Fig. 4. Same X-ray mosaic as Fig. 1 smoothed to match the Point Spread Function of the HESS telescopes. The scale is linear and units are in ph/cm^2/s/arcmin^2. Overlaid are the γ-ray contour excess (spaced at 30, 60 and 90 counts) from Fig. 7 of Aharonian et al. (2006). The sectors used for the radial profile comparison of Fig. 10 are also drawn.

bins of some X-ray profiles, there is not enough coverage to estimate the flux. Those bins are removed from the profile. As in the spectral study, the two brightest point-like sources (see Sect. 3.2) were removed from the X-ray images. The resulting radial profiles are shown in Fig. 10 and discussed in Sect. 4.3.2.

4. Results

4.1. Radio flux

An accurate estimate of the integrated radio flux density is critical to investigate the mechanisms responsible for the high-energy emission. In this work we re-analyze the available radio data at 1.4 GHz following two different paths to estimate the radio flux density of RX J1713.7-3946.

Since the largest well imaged structure for the ATCA observations is 25 arcmin in size, to recover information of structures larger than this size, the combination with single dish observations is required. However, in this case, it was not possible to complete the procedure due to the fact that the overlap annulus of the interferometric and single antenna data set[1] in the uv space is too small to produce a reliable image. We therefore used the single dish data at 1.4 GHz to estimate the integrated flux density within the area covered by the X-ray emission associated with the SNR (outer contour depicted in Fig. 5). This estimate provides an upper limit for the flux density of about 26 Jy with an uncertainty of the order of 10%. In addition we integrated over an interferometric image based on ATCA data within the same outer contour. In this case, since the largest well imaged structure at this frequency is about 25 arcmin, we corrected "by hand" adding the minimum flux density required to fill in the few negatives remaining in the image. The surface brightness corresponding to this addition was below 7.4×10^{-24} W m^{-2} Hz-1 sr^{-1}. The off-source rms-noise is about 0.7 mJy/beam and the constant value added to fill in the few negatives is 1.2 mJy/beam. Such correction amounts less than 1% of the total estimated flux density.

Whether the radio emission from Arc 2 (see Fig. 5) is thermal or non-thermal in nature is an important issue as it is one the brightest features within the X-ray contours. In order to investigate the connection of Arc 2, with the SNR, we used mid-infrared observations. The right-hand panel of Fig. 5 shows *Spitzer* 8 μm mid-infrared emission in the direction of RX J1713.7-3946. Particularly, it can be seen intense infrared emission at the location of the HII region G347.611+0.204. The infrared emission also evidences good morphological correlation with the radio Arc 2 suggesting a thermal origin for this feature. To investigate the nature of Arc 2 we applied the color-color criteria proposed by Reach et al. (2006) based on *Spitzer* data obtained at 3.6, 4.5, 5.8, and 8 μm, finding that Arc 2 has color characteristics compatible with polycyclic aromatic hydrocarbons (PAHs) origin (see Fig. 6). Besides we applied HI ab-

[1] The only public single dish data available at this frequency come from the Survey of the South Celestial Hemisphere carried out with the 30 m dish of the Argentine Institute of Radio Astronomy (IAR Testori et al. 2001) (HPBW~34 arcmin at 1.4 GHz)

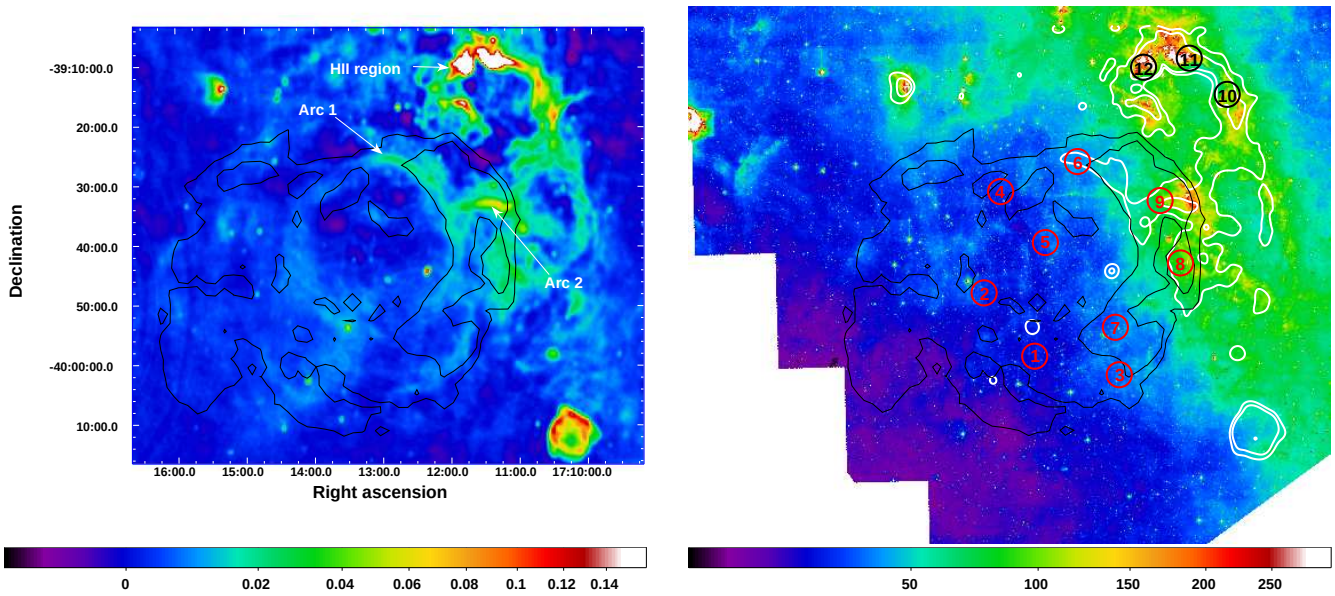

Fig. 5. *Left* : Radio image of the region of RX J1713.7-3946 at 1.4 GHz (from Lazendic et al. 2004). The scale is square root and units are in Jy beam^{-1}. *Right* : *Spitzer* image at 8 μm from the GLIMPSE survey. The X-ray contours are represented in black in both images and the radio contours in white. The regions used for the color-color plot of Fig. 6 are labeled here. The scale is square root and units are in MJy sr^{-1}.

sorption techniques based on data extracted from the Southern Galactic Plane Survey (SGPS; McClure-Griffiths et al. 2005) together with a flat rotation model for our Galaxy (assuming as solar parameters $R_\odot = 7.6 \pm 0.3$ kpc and $\Theta_\odot = 214 \pm 7$ km s^{-1}). From this study we conclude that the most distant HI absorption feature for the Arc 2 is at -120 km/s, which corresponds to a near distance of $\sim$ 6.7 kpc, placing in principle this thermal arc beyond RX J1713.7-3946. With this information, to estimate the associated radio flux density we subtracted the contribution from all overlapping radio point sources (likely to be extragalactic and/or compact HII regions) and from Arc 2 (about 1.5 Jy) because it is likely to be unrelated with the remnant, estimating a lower limit for the total flux density of $\sim$ 22 Jy. Therefore, we conclude that the associated radio flux density at 1.4 GHz is between 22 and 26 Jy.

4.2. Global X-ray flux

We extracted a MOS spectrum from the whole remnant without degrading the spatial resolution of the data. The best-fit parameters (with background subtraction as described in Sect. 3.3) are $N_{\rm H} = 0.66 \pm 0.01 \times 10^{22}$ cm^{-2}, index=2.37 $\pm$ 0.01, an absorbed 1-10 keV flux of 3.95 $\pm 0.03 \times 10^{-10}$ erg cm^{-2}s^{-1} and a non absorbed flux in the same band of 5.23 $\pm 0.04 \times 10^{-10}$ erg cm^{-2}s^{-1}. Our main source of uncertainty is the absolute calibration of *XMM-Newton* which is known with a precision of 10% rather than the very small statistical error (less than 1%). Another flux estimate is obtained with a srcut synchrotron model using the radio flux upper limit derived in Sect. 4.1. The non absorbed flux derived is 5.49 $\pm 0.05 \times 10^{-10}$ erg cm^{-2}s^{-1}, very similar to the one obtained with a power law model. In the *srcut* model, the radio spectral index was fixed to 0.6 and a break frequency of 4.2 $\times 10^{17}$ Hz was derived. This value, averaged across the remnant, is similar to the maximum break frequency reached in the bright limbs of SN 1006 (Rothenflug et al. 2004).

We note that the 1-10 keV non absorbed flux obtained by Tanaka et al. (2008) with *Suzaku* is 47% higher (7.65 $\times 10^{-10}$ erg cm^{-2}s^{-1}) than what we have found. However the absorption and index of their spectrum (0.79×10^{22} cm^{-2} and 2.39 respectively) are in agreement with our parameters. It is important to note that whereas our spectrum is extracted directly on the whole remnant, the *Suzaku* spectrum is the sum of spectra from 10 particular regions scaled up to the whole remnant assuming the surface brightness from the *ASCA* image (Sect. 3.3 of Tanaka et al. 2008). In our spectrum, the point sources were removed but their contribution to the total flux is weak (less than 1% for the Central Compact Object). We have cross checked the value of our absorbed global flux derived from the spectrum (in the 0.5-4.5 keV energy band) to the one derived from our mosaiced image. Both fluxes agree within 5%.

4.3. X- and γ-ray comparison

4.3.1. Spectral results

The best-fit parameters of the X-ray spectral modeling of the 14 regions are given in Table 2. The large variation of photon index ($1.9 < \Gamma < 2.6$) seen in X-rays when using small extraction regions in Cassam-Chenaï et al. (2004) have largely been reduced here with larger extraction regions and a degraded spatial resolution for the X-ray data ($2.2 < \Gamma < 2.4$, see Fig. 7). The comparison of the X- and γ-ray photon index (Fig. 8) shows no significant correlation . The distribution of the photon index in X- and γ-rays has a mean value of 2.32 and 2.09 respectively and a standard deviation of 0.075 and 0.073. Whereas the dispersion of the photon index at both energies is the same, the X-ray index is slightly higher than the γ-ray one. However, there is a systematic error on the γ-ray photon index of 0.1 (AH06) that is to be added to the Fig.8. Whereas the variations of the photon index are small, there are significant variations in the flux from the 14 large regions. Fig. 9 shows a good correlation between the X-

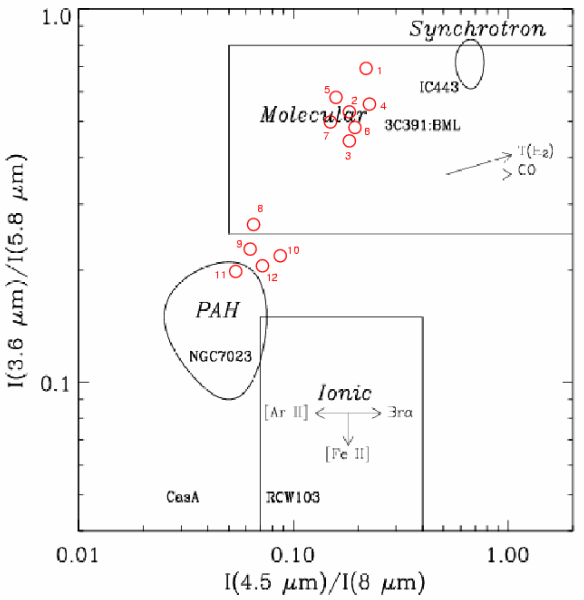

Fig. 6. Infrared color-color diagram for the regions defined in Fig. 5 (*Right*) overlaid on Fig. 2 of Reach et al. (2006). Two distincts groups can be seen. The emission from the regions 8 to 12 is compatible with PAH origin including our region of interest Arc 2 (labeled as region 9 here). Therefore the radio emission from Arc 2 is likely to be thermal and not related with the remnant.

Table 2. Best-fit X-ray parameters obtained with an absorbed power law model for the HESS regions defined in Fig. 2. The X-ray flux is integrated in the 1-10 keV band.

Region	N_H 10^{22}cm^{-2}	Index	Integrated flux[a] (10^{-2}cm^{-2}s^{-1})
1	0.79	2.43 (2.42-2.44)	0.91 (0.90-0.92)
2	0.62	2.35 (2.34-2.35)	1.58 (1.57-1.59)
3	0.72	2.35 (2.35-2.36)	1.74 (1.73-1.75)
4	0.76	2.37 (2.37-2.39)	0.76 (0.75-0.77)
5	0.59	2.32 (2.31-2.32)	1.42 (1.41-1.43)
6	0.56	2.44 (2.43-2.44)	1.44 (1.43-1.45)
7	0.67	2.41 (2.40-2.42)	0.89 (0.87-0.90)
8	0.64	2.23 (2.22-2.24)	0.58 (0.57-0.58)
9	0.48	2.22 (2.22-2.23)	0.90 (0.89-0.91)
10	0.46	2.32 (2.31-2.33)	1.15 (1.14-1.16)
11	0.63	2.35 (2.34-2.36)	0.72 (0.72-0.74)
12	0.50	2.17 (2.15-2.18)	0.51 (0.50-0.52)
13	0.51	2.31 (2.30-2.32)	0.69 (0.68-0.70)
14	0.57	2.28 (2.26-2.29)	0.70 (0.68-0.70)

[a] Corrected for absorption

ray integrated flux (1-10 keV band) and the γ-ray integrated flux (1-10 TeV band). We note that the bright regions are brighter in X-rays than in γ-rays. Such a behaviour has also been observed by Tanaka et al. (2008) with *Suzaku*. However whereas they interpreted this as a linear correlation with some X-ray deviation, we interpret this as a non-linear correlation. We measured this non-linear correlation placing the X-ray flux in the X axis (as the error bars on the X-ray flux are smaller than those in γ-rays). This measured slope is then inverted to obtain $\mathrm{d}\log F_\nu^{\mathrm{X}}/\mathrm{d}\log F_\nu^{\gamma}$. The best-fit power law function $F_\nu^{\mathrm{X}} = 0.81 \pm 0.09\,(F_\nu^{\gamma})^{2.41\pm0.55}$ is

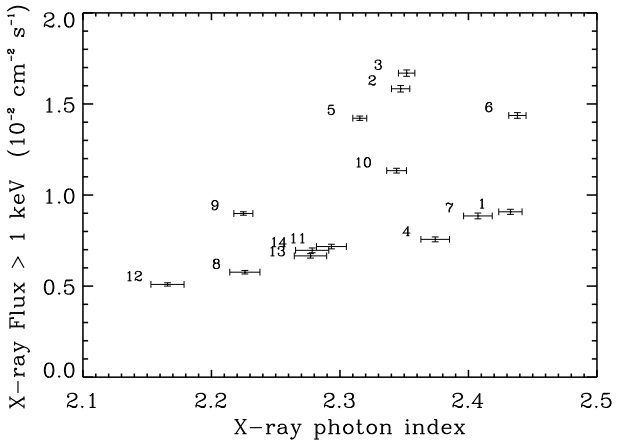

Fig. 7. Correlation plot between the X-ray photon index and the X-ray integrated flux (in the 1-10 keV band). The parameters shown here are the average of MOS1 and MOS2 best-fit parameters. The label over each point corresponds to HESS regions as defined in Fig. 2.

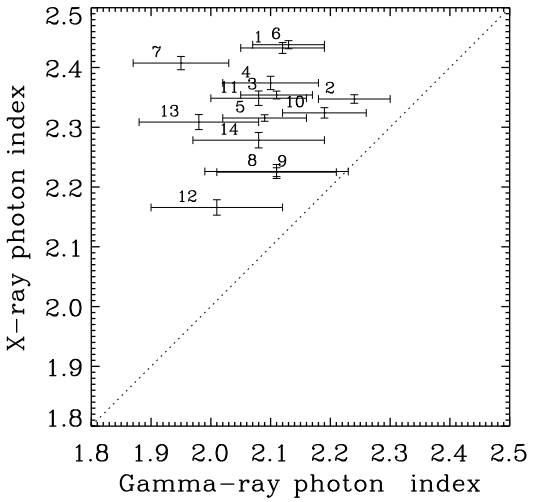

Fig. 8. X-ray photon index against γ-ray photon index. A systematic error of 0.1 is to be added to the γ-ray photon index. The dashed line is the bisector.

statistically preferred ($\chi^2/d.o.f. = 9.28/12$) over the best-fit linear function $F_\nu^{\mathrm{X}} = 1.01 \pm 0.04\,F_\nu^{\gamma}$ ($\chi^2/d.o.f. = 61.06/13$). We note that the fit with a linear function $F_\nu^{\mathrm{X}} = aF_\nu^{\gamma} - b$ (bestfit parameters : $a = 2.26$ and $b = 1.43$) gives similar results in term of χ^2 ($\chi^2/d.o.f. = 9.38/12$) than the non-linear fit but is not physically understandable since both images are already background subtracted.

4.3.2. Morphological results

The comparison of the radial profiles allows us to investigate the extent of each emission as well as to localize their respective peaks. Such a study has already been carried out by AH06 by comparing the ASCA and HESS data. However as the coverage with ASCA did not always reach the boundaries of the SNR it was not possible to compare the extension of the remnant in both wavelengths.

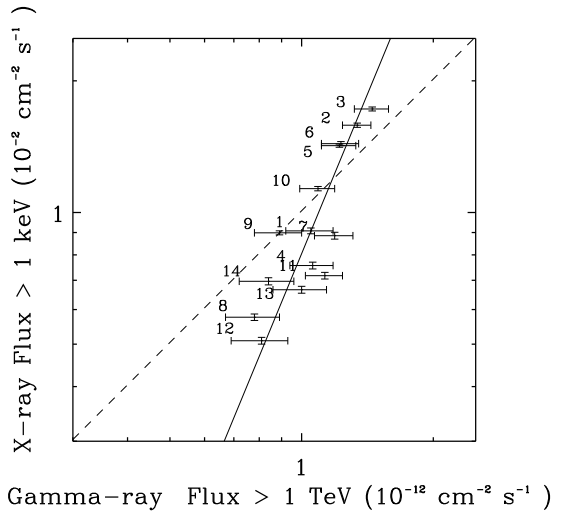

Fig. 9. Log-log correlation plot between the HESS γ-ray integrated flux (1-10 TeV band) and the *XMM-Newton* X-ray integrated flux (1-10 keV band, using MOS1&2 data). We can see that the correlation is best-fitted with a non-linear function $F_\nu^{\rm X} = 0.81 \pm 0.09\,(F_\nu^\gamma)^{2.41\pm0.55}$ (solid line). The best-fit linear function $F_\nu^{\rm X} = 1.01 \pm 0.04\,F_\nu^\gamma$ is also represented (dashed line).

The global agreement in the 8 sectors is good and particularly striking in sector 7 (the brightest spot of the remnant in both wavelength) as can be seen in Fig. 10. In regions 5 and 6 we see that the peak of the emission, along the radial direction, is located closer to the center in X-rays than in γ-rays. The global shape of the radial profile is similar in both wavelength but shifted by $\sim$0.1° to the center in X-rays.

It is important to note that we did subtract an astrophysical background to the X-ray radial profiles. To estimate the background, we used the same region as in the mosaic building section (Sect. 3.1).

5. Discussion

5.1. Global synchrotron spectrum

The radio flux density at 1.4 GHz that we derive in our study (22 Jy < S < 26 Jy) for the whole remnant is significantly higher than the flux density previously published. However it is important to note that the flux calculated by Ellison et al. (2001) (S=4±1 Jy) was estimated only locally for the two bright arcs in the northwestern region. Later on, Lazendic et al. (2004) derived for these features a flux density of 6.7 ± 2.0 Jy based on the improved radio image at 1.4 GHz. In X-rays the contribution of the northwestern region accounts for $\sim$ 20 % of the total flux in the 0.5-4.5 keV energy band. If the ratio of synchrotron emission in X-rays to that in radio is more or less constant throughout the remnant, the radio flux expected for the whole remnant is of the order of 26 Jy[2] which is compatible with our estimation. We note that the flux that we derive is about 2 times higher than the flux of 13.4 Jy used in AH06. This flux density was obtained assuming that the flux density for the entire remnant was about twice the flux density value obtained by Lazendic et al. (2004) for the northwestern region. Our higher new estimate tend to reduce the difference between the measurements and predictions of the hadronic models usually requiring high magnetic fields > 100 μG (Tanaka et al. 2008).

In X-rays, the 1-10 keV non absorbed flux that we derive with *XMM-Newton* is significantly lower than the value derived by Tanaka et al. (2008) with *Suzaku* (5.23 and 7.65 $\times 10^{-10}$ erg cm^{-2}s^{-1} respectively, see Sect. 4.2). This new X-ray flux together with the higher radio flux estimate decrease the global X-ray to radio ratio by about a factor of 3. Such a change is clearly important in the shape of the synchrotron spectral energy distribution and could impact the results from multi-wavelength models of the remnant.

5.2. X- and γ-ray comparison

5.2.1. Spectral index

When using large extraction regions and degrading the spatial resolution of the X-ray data, we found no significant spatial variation of the photon index (see Sect. 4.3.1). In other words, the small-scale variations reported by Cassam-Chenaï et al. (2004) are washed out at the resolution of the HESS telescope. If there exists small-scale spectral variations in γ-rays, one expect them to be washed out as well with the current HESS resolution. However the mean X-ray photon index (2.32) is slightly steeper than the γ-ray one (2.09). In the case of IC off the CMB photons for the γ-ray emission, the mean electron energy required to have a photon at 1 TeV is $E_{\rm e}^{\rm IC}$= 16 TeV (for IC off IR or optical photons it is of course lower). The electrons emitting synchrotron at 1 keV with a magnetic field of 70 μG have an energy of $E_{\rm e}^{\rm sync}$= 27 TeV. At those energies the electrons are close to the cutoff and we do expect a higher index when looking at electrons of higher energies. We can reasonably set an upper limit to the magnetic field as $E_{\rm e}^{\rm sync}$ cannot be lower than $E_{\rm e}^{\rm IC}$ in order to reproduce the steeper index of the synchrotron spectra. This sets an upper limit on the downstream magnetic field of 200 μG, consistent with the estimate coming from the width of the X-ray filaments (about 70 μG from Ballet 2006; Berezhko & Völk 2006).

5.2.2. Correlation between the X-ray and γ-ray fluxes.

We have found in Sect. 4.3.1 that the X-ray flux is indeed correlated with the γ-ray flux, but the correlation appears non-linear, more like $\mathrm{d}\log F_\nu^{\rm X}/\mathrm{d}\log F_\nu^\gamma = 2.41 \pm 0.55$ (Fig. 9). We discuss here why it could be so. We will assume that most of the range in flux that we see is due to density variations around the remnant. It is certainly not entirely true (geometric effects such as limb brightening must play a role at some point) but it is probably indeed the major contributor in view of the very structured interstellar gas and X-ray image. We will assume that in the range which emits the γ and X-ray (*i.e.* one to a few hundred TeV) the particle distribution can be represented as a cut-off power law $dN/dE = KE^{-s}C(-E/E_{\rm c})$ in which K is proportional to the ambient density and $E_{\rm c}$ is limited by synchrotron losses for electrons ($E_{\rm c,e} \propto V_{\rm sh}/\sqrt{B_{\rm d}}$) and by age for protons ($E_{\rm c,p} \propto B_{\rm d}V_{\rm sh}^2$) where $B_{\rm d}$ is the downstream magnetic field. The shape of the cutoff C(x) can be any function decreasing from 1 to 0. We will further assume that magnetic field may increase with density ($B_{\rm d} \propto n^\beta$) and that the shock velocity adjusts as $V_{\rm sh} \propto n^{-0.5}$ (same pressure).

[2] Without taking into account the thermal emission from Arc 2 that accounts for about 1.5 Jy out of the 6.7 Jy estimation from Lazendic et al. (2004).

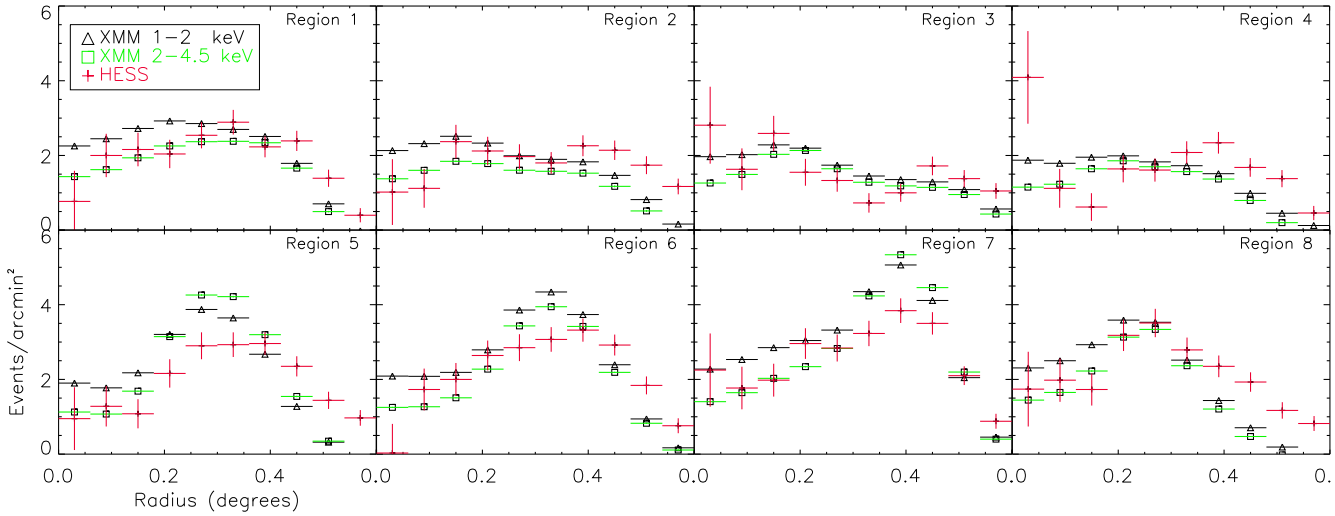

Fig. 10. Radial profiles in X-rays in two energy bands and in γ-rays for the 8 sectors defined in Fig. 4. The general agreement is good and particularly striking in sector 7 (the brightest spot of the remnant in both wavelengths). However there are also interesting differences in sectors 5 and 6 where the bulk of the X-ray emission seems to come more from the inside of the SNR than in γ-rays.

By calculating $\mathrm{d}\log F_\nu/\mathrm{d}\log n$ for the synchrotron and Inverse Compton case (see Appendix A), we can then predict in the flux-flux correlation comparable to Fig. 9 :

$$\frac{\mathrm{d}\log F_\nu^{\mathrm{sync}}}{\mathrm{d}\log F_\nu^{\mathrm{IC}}} = \frac{\frac{s+1}{2}(1+\beta)-\alpha_X}{1-(1+\beta)(\alpha_\gamma-\frac{s-1}{2})} \quad (1)$$

where α_X and α_γ are respectively the X and γ-ray spectral slope in energy not photons ($\alpha_i = -\mathrm{d}\log F_\nu^i/\mathrm{d}\log\nu$).

For a standard value of $s = 2$ and the observed values of α_X = 1.32 and α_γ = 1.09 this gives (0.18 + 1.5 β) / (0.41 - 0.59 β). If B_d is insensitive to density ($\beta = 0$) the predicted correlation is opposite of what is seen: the range in X-ray flux would be smaller than in γ-rays, because the negative feedback on ν_c via V_sh plays more strongly in X-rays which are further in the cutoff part of the spectrum. But a modest dependence of B_d on density like $\beta = 0.1$ is enough to invert the trend because in the loss-dominated regime the γ-ray cutoff frequency decreases with B_d while the X-ray one is independent of B_d. In other words, the slope of the log(F_X) vs log(F_γ) correlation is very sensitive to β. To get the observed value of 2.41 requires $\beta = 0.28$.

In view of the oversimplified character of that approach we do not claim that this is a measurement of $\mathrm{d}\log B_\mathrm{d}/\mathrm{d}\log n$ but we think it shows that such a steep correlation is reasonable in a leptonic model. The specific model in which we have tried to push the calculation further (Appendix B) does not give a consistent answer, but it is far from unique. One way to improve on the measurements would be to use extraction areas in which the filling factor of the SNR is the same, like the angular sectors on Fig.4. This would leave in the flux variations only what is due to varying external conditions. It requires reanalyzing the HESS data, so it is left for future work.

If we now turn to the hadronic hypothesis, the same line of reasoning (see Appendix A) then leads to :

$$\frac{\mathrm{d}\log F_\nu^{\mathrm{sync}}}{\mathrm{d}\log F_\nu^{\mathrm{hadr}}} = \frac{\frac{s+1}{2}(1+\beta)-\alpha_X}{2-(1-\beta)(\alpha_\gamma+1-s)} \quad (2)$$

For a standard value of $s = 2$ and the observed values of α_X = 1.32 and α_γ = 1.09 this gives (0.18 + 1.5 β) / (1.91 + 0.09 β). It is clear that whatever $\beta < 1$ (it is hard to imagine how B_d could increase faster than density) this quantity is always < 1. In other words, no magnetic field can make up for the natural n^2 character of the hadronic mechanism which predicts a fast increase of F_ν^{hadr} with density. So at least in that (over)simplified framework the correlation we observe is not in favor of a hadronic model.

There remains the possibility (Malkov et al. 2005) that the density increases very fast outwards (SNR hitting a shell) to the point where most of the γ-ray emission arises outside the remnant (in the precursor). In that case the width of the precursor increases as E so that the spectral shape of the γ-ray emission may be estimated by multiplying F_ν^{hadr} by E (Zirakashvili & Aharonian 2007). This in turn changes (2) into

$$\frac{\mathrm{d}\log F_\nu^{\mathrm{sync}}}{\mathrm{d}\log F_\nu^{\mathrm{hadr}}} = \frac{\frac{s+1}{2}(1+\beta)-\alpha_X}{2-(1-\beta)(\alpha_\gamma+2-s)} \quad (3)$$

so that for $s = 2$ and the observed spectral indices one expects (0.18 + 1.5 β) / (0.91 + 1.09 β) for the slope of the log(F_X) vs log(F_γ) correlation. This is still always < 1.

5.3. Spatial comparison

The main difficulty of a leptonic model to account for the observations in RX J1713.7-3946 is that it requires a small magnetic field (on the order of 10 μG ; AH06) to explain the rather large γ to X-ray ratio, if the emitting volume is the same. This is inconsistent with the magnetic field derived from the width of the X-ray filaments (70 μG or so). A possible reason, suggested by Lazendic et al. (2004), is that the magnetic turbulence decays behind the shock faster than the electrons lose energy. This leaves a larger volume (downstream) to IC than synchrotron, and does not require that large a magnetic field to begin with. A definite prediction is then that the γ-ray emission should peak inside the X-rays.

In the comparison of the X- and γ-ray radial profiles (4.3.2) we did see a radial shift, particularly visible in region 6 (West), between the X- and γ-ray emission. But the shift is in the opposite direction, *i.e.* the X-ray emission peaks at smaller radius than the γ-ray emission. The value of this shift for region 6 is

$\sim 0.06^\circ$=1.2 pc with a remnant at 1 kpc. Another effect that we have not discussed is that because of the magnetic jump at the shock (typically a factor 3 if the magnetic field is mostly turbulent and isotropic), the synchrotron emission is strongly suppressed ahead of the shock whereas the IC emission will decrease more smoothly over one diffusion length. In a Bohm regime the diffusion coefficient is $D_{\rm B} = r_{\rm L}c/3$ where $r_{\rm L}$ is the Larmor radius and the diffusion length $l_{\rm diff} = D_{\rm B}/V_{\rm sh}$ where $V_{\rm sh}$ is the shock wave velocity. For an electron energy of 16 TeV, a shock speed of 4000 km/s and an upstream magnetic field of 10 μG we have $l_{\rm diff} = 0.1$ pc. This is small in comparison with the shift of 1.2 pc.

However there exists another purely geometric possibility to explain why the X-rays peak inside the γ-rays. Actually from Fig.10 the effect is significant only in regions 6 (West) and 8 (North). In both regions it looks from the image (Fig.1) that the remnant extends beyond the main X-ray peak. This is typical of a line of sight superposition of a region with larger density (brighter, slower shock) and a region of lower density (fainter, faster shock). This idea is supported by the fact that observations in CO (Moriguchi et al. 2005) show that clouds are present in those particular regions. Now from Fig.7 we know that the X-ray brightness increases much faster than the γ-ray brightness. The X-ray radial profile is then dominated by the inner bright edge, whereas the outer plateau may contribute significantly to the γ-ray emission and shift the integral along the line of sight to a larger radius. Because of that possibility we cannot say that the radial profile is incompatible with a leptonic model.

In a hadronic model the simplest way to understand that the γ-ray emission is further out is if a sizable fraction of the flux comes from outside the shock. This is possible and actually expected (Malkov et al. 2005) if the ambient density increases ahead of the shock (SNR entering a molecular cloud). There are then vast amounts of upstream gas to be used as targets for accelerated protons. A definite prediction of that model is that the remnant should look larger as energy increases because it will be governed by the diffusion length. The energy range in the HESS data may be enough to test that, and certainly will after HESS 2.

6. Summary

New *XMM-Newton* observations of RX J1713.7-3946 have allowed us to complete the coverage of the remnant. We have then carried out a comparison of the remnant in X- and γ-rays. The radio emission has also been studied. This leads us to the following conclusions :

1. The small scale variations of the X-ray photon index are largely smeared out at the resolution of the HESS telescope. This is consistent with the non detection of photon index variation in the γ-rays.
2. The mean X-ray photon index (2.32) is slightly steeper than the γ-ray one (2.09). This is expected in a leptonic scenario as the electrons emitting γ-ray Inverse Compton have a lower energy than those emitting X-ray synchrotron. The photon index offset is thus the result of the spectrum cutoff of the electrons.
3. The comparison of the X-ray vs γ-ray integrated flux suggests a non-linear correlation with $\mathrm{d}\log \mathrm{F}_\nu^{\rm X}/\mathrm{d}\log \mathrm{F}_\nu^{\gamma} = 2.41 \pm 0.55$. If the range of flux that we see is due to the variation of the density around the remnant then a leptonic model can more easily reproduce the observed X/γ-ray correlation.
4. The comparison of the radial profile in X- and γ-rays indicates that for some regions, the X-ray emission comes more from the inside of the remnant than in γ-rays. This can be explained in a hadronic model if a fraction of the γ-ray flux comes from the outside of the remnant (interaction of the remnant with a cloud). However this radial shift could also be due to superposition effects. Therefore we can not rule out the leptonic scenario.
5. Concerning the radio counterpart of the remnant, we have shown that one of the brightest arcs seen at 1.4 GHz (Arc 2) is of thermal origin and likely not associated with the remnant. Taking this into account, we have derived a lower limit on the integrated flux density of 22 Jy and an upper limit of 26 Jy.

Acknowledgements. This project was partially funded by ECOS-SUD France-Argentina A04U03 program and ANPCYT, CONICET and UBACYT (Argentina) grants. G. Dubner and E. Giacani are members of CONICET (Argentina). M. Ortega is a Doctoral Fellow of CONICET (Argentina).

References

Aharonian, F., Akhperjanian, A. G., Bazer-Bachi, A. R., et al. 2006 (AH06), A&A, 449, 223
Aharonian, F. A., Akhperjanian, A. G., Aye, K.-M., et al. 2004, Nature, 432, 75
Arnaud, M., Neumann, D. M., Aghanim, N., et al. 2001, A&A, 365, L80
Ballet, J. 2006, Advances in Space Research, 37, 1902
Benjamin, R. A., Churchwell, E., Babler, B. L., et al. 2003, PASP, 115, 953
Berezhko, E. G. & Völk, H. J. 2006, A&A, 451, 981
Carter, J. A. & Read, A. M. 2007, A&A, 464, 1155
Cassam-Chenaï, G., Decourchelle, A., Ballet, J., et al. 2004, A&A, 427, 199
Conti, P. S. & Crowther, P. A. 2004, MNRAS, 355, 899
Ellison, D. C., Slane, P., & Gaensler, B. M. 2001, ApJ, 563, 191
Enomoto, R., Tanimori, T., Naito, T., et al. 2002, Nature, 416, 823
Fukui, Y., Moriguchi, Y., Tamura, K., et al. 2003, PASJ, 55, L61
Hiraga, J. S., Uchiyama, Y., Takahashi, T., & Aharonian, F. A. 2005, A&A, 431, 953
Koyama, K., Kinugasa, K., Matsuzaki, K., et al. 1997, PASJ, 49, L7
Lazendic, J. S., Slane, P. O., Gaensler, B. M., et al. 2003, ApJ, 593, L27
Lazendic, J. S., Slane, P. O., Gaensler, B. M., et al. 2004, ApJ, 602, 271
Malkov, M. A., Diamond, P. H., & Sagdeev, R. Z. 2005, ApJ, 624, L37
McClure-Griffiths, N. M., Dickey, J. M., Gaensler, B. M., et al. 2005, ApJS, 158, 178
Moriguchi, Y., Tamura, K., Tawara, Y., et al. 2005, ApJ, 631, 947
Muraishi, H., Tanimori, T., Yanagita, S., et al. 2000, A&A, 354, L57
Pannuti, T. G., Allen, G. E., Houck, J. C., & Sturner, S. J. 2003, ApJ, 593, 377
Pfeffermann, E. & Aschenbach, B. 1996, in Roentgenstrahlung from the Universe, ed. H. U. Zimmermann, J. Trümper, & H. Yorke, 267–268
Pratt, G. W. & Arnaud, M. 2002, A&A, 394, 375
Reach, W. T., Rho, J., Tappe, A., et al. 2006, AJ, 131, 1479
Rothenflug, R., Ballet, J., Dubner, G., et al. 2004, A&A, 425, 121
Russeil, D. 2003, A&A, 397, 133
Slane, P., Gaensler, B. M., Dame, T. M., et al. 1999, ApJ, 525, 357
Tanaka, T., Uchiyama, Y., Aharonian, F. A., et al. 2008, ApJ, 685, 988
Testori, J. C., Reich, P., Bava, J. A., et al. 2001, A&A, 368, 1123
Wang, Z. R., Qu, Q. Y., & Chen, Y. 1997, A&A, 318, L59
Zirakashvili, V. N. & Aharonian, F. 2007, A&A, 465, 695

Appendix A: Correlation between the X-ray and γ-ray fluxes

The synchrotron emission can be written

$$F_\nu^{\rm sync} \propto K_{\rm e}\, B^{\frac{s+1}{2}}\, \nu^{-\frac{s-1}{2}}\, S\left(\frac{\nu}{\nu_{\rm c}^{\rm sync}}\right) \tag{A.1}$$

where S is a function characteristic of synchrotron emission and the shape of the electron cutoff and $\nu_{\rm c}^{\rm sync} \propto BE_{\rm c,e}^2 \propto V_{\rm sh}^2$. Then

$$\frac{\mathrm{d}\log F_\nu^{\rm sync}}{\mathrm{d}\log n} = 1 + \frac{s+1}{2}\beta - \frac{S'}{S}\,\frac{\nu}{\nu_{\rm c}^{\rm sync}}\,\frac{\mathrm{d}\log \nu_{\rm c}^{\rm sync}}{\mathrm{d}\log n} \tag{A.2}$$

Noting that

$$\frac{\mathrm{d}\log F_\nu^{\rm sync}}{\mathrm{d}\log\nu} = -\frac{s-1}{2} + \frac{S'}{S}\,\frac{\nu}{\nu_{\rm c}^{\rm sync}} = -\alpha_X \tag{A.3}$$

is the X-ray spectral slope (in energy, not photons) and that $\mathrm{d}\log\nu_{\rm c}^{\rm sync}/\mathrm{d}\log n = -1$, we can write

$$\frac{\mathrm{d}\log F_\nu^{\rm sync}}{\mathrm{d}\log n} = 1 + \frac{s+1}{2}\beta - \alpha_X + \frac{s-1}{2} = \frac{s+1}{2}(1+\beta) - \alpha_X \tag{A.4}$$

As long as the Klein-Nishina reduction of the cross-section is not reached (this is still true for 10 TeV electrons on the CMB) the Inverse Compton emission may be written in the same way as (A.1) but without any explicit B term and with $\nu_{\rm c}^{\rm IC} \propto E_{\rm c,e}^2 \propto V_{\rm sh}^2/B$. The same line of reasoning then leads to

$$\frac{\mathrm{d}\log F_\nu^{\rm IC}}{d\log n} = 1 - (1+\beta)\left(\alpha_\gamma - \frac{s-1}{2}\right) \tag{A.5}$$

in which α_γ is the γ-ray spectral slope.

Putting together (A.4) and (A.5) we then predict in the flux-flux correlation comparable to Fig.9

$$\frac{\mathrm{d}\log F_\nu^{\rm sync}}{\mathrm{d}\log F_\nu^{\rm IC}} = \frac{\frac{s+1}{2}(1+\beta) - \alpha_X}{1 - (1+\beta)(\alpha_\gamma - \frac{s-1}{2})} \tag{A.6}$$

If we now turn to the hadronic hypothesis, the π^0 decay emission may be written

$$F_\nu^{\rm hadr} \propto K_{\rm p}\, n\, \nu^{1-s}\, H\left(\frac{\nu}{\nu_{\rm c}^{\rm hadr}}\right) \tag{A.7}$$

where H is a function characteristic of π^0 emission and the shape of the proton cutoff and $\nu_{\rm c}^{\rm hadr} \propto E_{\rm c,p} \propto BV_{\rm sh}^2$. The same line of reasoning then leads to

$$\frac{\mathrm{d}\log F_\nu^{\rm hadr}}{\mathrm{d}\log n} = 2 - (1-\beta)(\alpha_\gamma + 1 - s) \tag{A.8}$$

in which we now assume that hadronic emission dominates the γ-ray spectral slope. Putting together (A.4) and (A.8) we then predict for the flux-flux correlation in the hadronic model

$$\frac{\mathrm{d}\log F_\nu^{\rm sync}}{\mathrm{d}\log F_\nu^{\rm hadr}} = \frac{\frac{s+1}{2}(1+\beta) - \alpha_X}{2 - (1-\beta)(\alpha_\gamma + 1 - s)} \tag{A.9}$$

There remains the possibility (Malkov et al. 2005) that the density increases very fast outwards (SNR hitting a shell) to the point where most of the γ-ray emission arises outside the remnant (in the precursor). In that case the width of the precursor increases as E so that the spectral shape of the γ-ray emission may be estimated by multiplying A.7 by E (Zirakashvili & Aharonian 2007).

This in turn changes (A.8) into

$$\frac{\mathrm{d}\log F_\nu^{\rm hadr}}{\mathrm{d}\log n} = 2 - (1-\beta)(\alpha_\gamma + 2 - s) \tag{A.10}$$

and changes (A.9) into

$$\frac{\mathrm{d}\log F_\nu^{\rm sync}}{\mathrm{d}\log F_\nu^{\rm hadr}} = \frac{\frac{s+1}{2}(1+\beta) - \alpha_X}{2 - (1-\beta)(\alpha_\gamma + 2 - s)} \tag{A.11}$$

Appendix B: Detailed calculation for electrons dominated by radiative losses

If the cutoff in the electron spectrum is defined by synchrotron cooling as we assume in Sect.5.2.2 and App.A, then the cooling continues downstream and the electron distribution integrated over space gets steeper (the power law index increases by 1) down to a break energy $E_{\rm b} \propto B^{-2}t_0^{-1}$ in which t_0 is the SNR age (Zirakashvili & Aharonian 2007). Since we are interested only in what happens above $E_{\rm b}$ this can be accounted for in (A.1) by changing s to the steeper value and considering that the normalization K_e follows $E_{\rm b}$ (the total number of electrons is always dominated by those below $E_{\rm b}$) or B^{-2} (t_0 is the same in all parts of the SNR). This amounts to adding -2β to Eqs (A.4) and (A.5), resulting in

$$\frac{\mathrm{d}\log F_\nu^{\rm sync}}{\mathrm{d}\log n} = \frac{s+1}{2} - \alpha_X + \frac{s-3}{2}\beta \tag{B.1}$$

$$\frac{\mathrm{d}\log F_\nu^{\rm IC}}{\mathrm{d}\log n} = \frac{s+1}{2} - \alpha_\gamma - \beta\left(\alpha_\gamma + \frac{5-s}{2}\right) \tag{B.2}$$

For the most interesting case $s = 3$ we then have

$$\frac{\mathrm{d}\log F_\nu^{\rm sync}}{\mathrm{d}\log F_\nu^{\rm IC}} = \frac{2 - \alpha_X}{2 - \alpha_\gamma - \beta(\alpha_\gamma + 1)} \tag{B.3}$$

For $\alpha_X = 1.32$ and $\alpha_\gamma = 1.09$ we get $0.68/(0.91 - 2.09\,\beta)$. This is very different from what is obtained with $s = 2$ and no break in the electron spectrum, but reaches the observed value 2.41 for a very similar value of $\beta = 0.30$.

The pion decay emission is insensitive to synchrotron cooling so that "radiative" model would predict $\mathrm{d}\log F_\nu^{\rm sync}/\mathrm{d}\log F_\nu^{\rm hadr} = 0.68/(1.91 + 0.09\,\beta)$. This is again always less than 1.

The same framework also naturally predicts variations of the spectral index going with the flux variations. Computing that requires a specific representation of the spectral shape. Suitable approximate formulae are given by Zirakashvili & Aharonian (2007) in their Eqs (35) and (46). They apply when there is no jump in magnetic field at the shock. This is not the most likely situation in our opinion, but it is still interesting to carry out the exercise to the end. The observed average spectral slope in X-rays $\alpha_X = 1.32$ corresponds to $x = \nu/\nu_{\rm c}^{\rm sync} = 4.5$, in keeping with what was derived by Tanaka et al. (2008) ($\nu_{\rm c}^{\rm sync} = 0.67$ keV). In the same way, the observed spectral slope in γ-rays $\alpha_\gamma = 1.09$ corresponds to $y = \nu/\nu_{\rm c}^{\rm IC} = 4.1$. From Eqs (34) and (45) of Zirakashvili & Aharonian (2007) we note that $\nu_{\rm c}^{\rm IC}/\nu_{\rm c}^{\rm sync} = (1.2$ TeV) / (2.2 keV) $(B/100\mu\mathrm{G})^{-1}$. For $B \simeq 70\,\mu$G and $\nu_{\rm c}^{\rm sync} = 0.67$ keV this predicts $\nu_{\rm c}^{\rm IC} \simeq 0.5$ TeV which is reasonable.

Coming back to the spectral index variations, since $\mathrm{d}\log\nu_{\rm c}^{\rm sync}/\mathrm{d}\log n = -1$ when it is limited by cooling, we have

$$\frac{\mathrm{d}\alpha_{\rm X}}{\mathrm{d}\log n} = -\frac{\mathrm{d}\alpha_{\rm X}}{\mathrm{d}\log x}\,\frac{\mathrm{d}\log\nu_{\rm c}^{\rm sync}}{\mathrm{d}\log n} = x\frac{\mathrm{d}\alpha_{\rm X}}{\mathrm{d}x} \tag{B.4}$$

$$\frac{\mathrm{d}\alpha_{\rm X}}{\mathrm{d}\log n} = 0.25\,x^{0.5} - 0.3795\,x^{0.6}\left(1 + 0.46\,x^{0.6}\right)^{-2} \tag{B.5}$$

At $x = 3.5$, this gives $\mathrm{d}\alpha_X/\mathrm{d}\log n = 0.32$. It then predicts $\mathrm{d}\log F_\nu^{\rm sync}/\mathrm{d}\alpha_X = 0.74 / 0.32 = 2.3$. The peak to peak dispersion that is observed on the X-ray flux $\Delta\log F_\nu^{\rm sync} \simeq 1.2$ should then be associated with a peak to peak dispersion on the slope $\Delta\alpha_X = 0.53$. This is larger than what is observed on Fig. 8 ($\Delta\alpha_X = 0.27$). This is qualitatively expected because flux variations are also affected by the geometry (the regions do not cover the same fraction of the SNR). However the small amplitude of the index variations implies that the fraction of the flux variations that is due

to geometry $\Delta \log F_\nu^{\rm geom}$ is large. It should add quadratically with the part due to density variations ($2.3 \times \Delta\alpha_X$) so $\Delta \log F_\nu^{\rm geom} \simeq 1.17$. Of course geometrical effects should affect the γ-ray emission in the same way but the observed dispersion on γ-ray flux is only $\Delta \log F_\nu^{\rm sync} \simeq 0.6$. This means we are at a dead-end. That specific model cannot explain at the same time the relatively uniform X-ray spectra and the larger contrast in the X-ray flux than the γ-ray flux.

Online Material

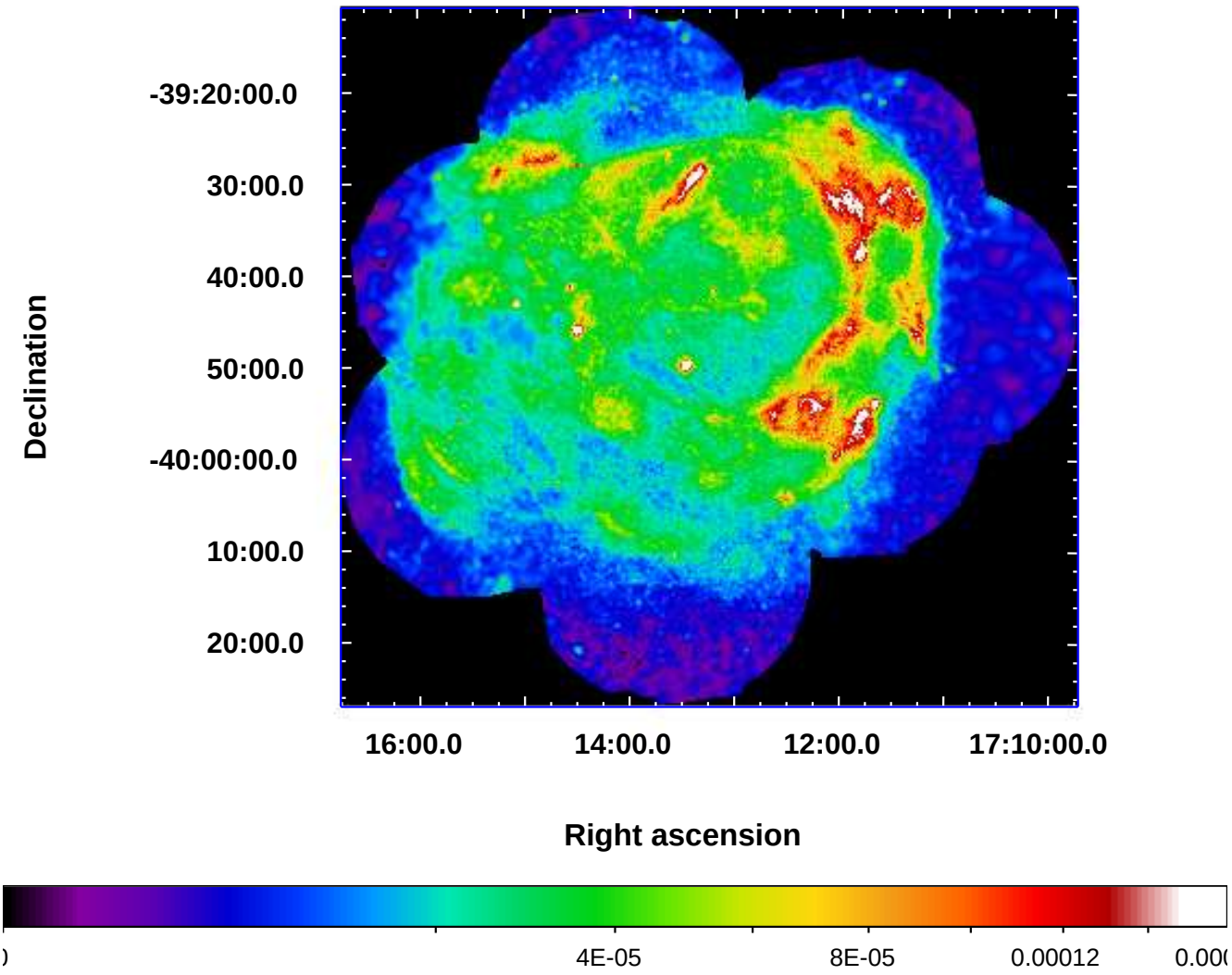

Fig. 1. EPIC MOS plus PN image in the 0.5-4.5 keV band. The units are ph/cm^2/s/arcmin^2 and the scale is square root. The image was adaptively smoothed to a signal-to-noise ratio of 10.